Integrating 3D Flower-Like Hierarchical Cu₂NiSnS₄ with Reduced Graphene Oxide as Advanced Anode Materials for Na-Ion Batteries

Shuang Yuan,[†,‡,§] Sai Wang,[†,‡,§] Lin Li,[†,‡] Yun-hai Zhu,[†,‡] Xin-bo Zhang,[*,†] and Jun-min Yan[*,‡]

[†]State Key Laboratory of Rare Earth Resource Utilization, Changchun Institute of Applied Chemistry, Chinese Academy of Sciences Changchun, 130022, China

[‡]Key Laboratory of Automobile Materials, Ministry of Education and School of Materials Science and Engineering, Jilin University, Changchun 130012, China

S *Supporting Information*
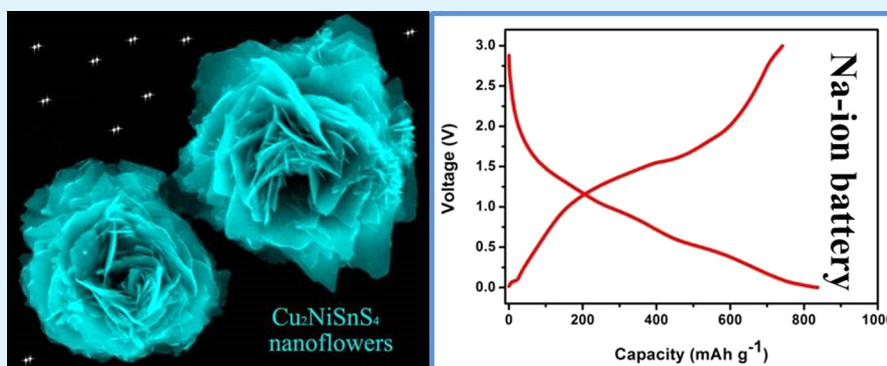
ABSTRACT: Development of an anode material with high performance and low cost is crucial for implementation of next-generation Na-ion batteries (NIBs) electrode, which is proposed to meet the challenges of large scale renewable energy storage. Metal chalcogenides are considered as promising anode materials for NIBs due to their high theoretical capacity, low cost, and abundant sources. Unfortunately, their practical application in NIBs is still hindered because of low conductivity and morphological collapse caused by their volume expansion and shrinkage during Na⁺ intercalation/deintercalation. To solve the daunting challenges, herein, we fabricated novel three-dimensional (3D) Cu₂NiSnS₄ nanoflowers (CNTSNs) as a proof-of-concept experiment using a facile and low-cost method. Furthermore, homogeneous integration with reduced graphene oxide nanosheets (RGNs) endows intrinsically insulated CNTSNs with superior electrochemical performances, including high specific capacity (up to 837 mAh g⁻¹), good rate capability, and long cycling stability, which could be attributed to the unique 3D hierarchical structure providing fast ion diffusion pathway and high contact area at the electrode/electrolyte interface.

KEYWORDS: *Na-ion batteries, Cu₂NiSnS₄, nanoflowers, graphene, anode*

■ INTRODUCTION

Earth abundant metal chalcogenides have attracted considerable attention owing to their broad applications in solar cells, light-emitting diodes, and battery electrodes.[1−3] As an important semiconductor, Cu₂NiSnS₄ (CNTS) is well-known for being one of the potential photovoltaic materials used in low-cost solar cells.[4−6] As a response, low-dimensional CNTS nanoparticles and nanorods have been synthesized due to their large absorb surface and fast electron transport properties.[4−6] Although there has been great progress with the preparation of CNTS, these methods still rely on toxic 3-mercaptopropionic acid, a high-temperature (more than 220 °C) or time-consuming (24 h) route, which intrinsically limits its large scale production. To date, CNTS with layered and tunneled structures have not been synthesized using environmentally friendly and low-cost precursors by any solvent methods, let alone CNTS with three-dimensional (3D) hierarchical nanosheets structure. Therefore, developing a facile, low-temperature, and time-saving approach for controlling the synthesis of CNTS with hierarchically nanostructure is highly desirable, but this remains a great challenge.

The worldwide application of lithium-ion batteries (LIBs) has facilitated unprecedented development of electronic gadgets.[7−12] However, to meet the future demands of large-scale electric energy storage application, we must consider the limited lithium reserve on the earth. Due to the inexhaustible sodium resources and similar electrochemical reaction mechanism, Na-ion batteries (NIBs) are a promising candidate to replace LIBs.[13−17] The CNTS with interlayer spaces and tunneled structure in its crystal structure makes it an ideal electrode material for high-performance NIBs.[18−21] Nevertheless, it is well-known that most metal sulfides suffer from low

electrical conductivity, large volume expansion, and poor kinetic problems during cycling in LIBs. This will result in fast capacity fade and poor rate capabilities in practice, to say nothing of NIBs.[22−24] Hence, considerable improvements in design and optimization of CNTS structure are still required before its application in NIBs. In response, construction of a hybrid material that combine hierarchically nanostructured CNTS and reduced graphene oxide nanosheets (RGNs) could potentially solve this problem.[25−28] The CNTS with hierarchical structure can provide fast ion diffusion pathway and high contact area at electrode/electrolyte interface. In addition, the RGNs can serve as highly conductive matrix and form a stable SEI film easily and significantly buffer volume expansion, which can effectively solve the kinetic problems.[25,26,29,30] Hence, developing a cost- and time-effective strategy to synthesize of CNTS/RGNs composite with nanostructure and investigating their application in NIBs are of great significance.

Herein, we demonstrated an effective and universal route to synthesize self-assembled 3D flower-like CNTS nanosheets (CNTSNs) with hierarchical architecture by phase controlling. Additionally, high electrochemical performances are obtained by constructing highly electric conductive RGN networks that ensure their desired homogeneous and intimate contact. When CNTSNs are employed as anode in NIBs, the advantageous combination of flexible and conductive RGNs with the as-prepared hierarchical CNTSNs shows good performances including high reversible capacity (837 mAh g^{-1}), cycling stability and good rate capability of 61 mAh g^{-1} at a high current density of 10 A g^{-1}.

■ RESULTS

Figure 1a shows the X-ray diffraction (XRD) patterns of obtained product. The products can be well indexed to diffractions of (111), (200), (220), (311), and (331) planes, respectively, of cubic CNTS phase (JCPDS 26-0552). No obvious peaks resulting from impurities are observed, indicating the high purity of the as-synthesized CNTS. The inset image is the schematic illustration of the CNTS structure, which can be described as 3D frameworks formed of $[Cu_2NiSnS_4]_n$ layers stacked parallel to the (110) plane.[1,6,31] In this framework, Cu/Ni/Sn atoms are connected by S to delineate irregular hexagon, which stack to form tunnels. The layers and tunnels could facilitate the insertion and extraction of guest species and more effectively buffer the volume change in the host during cycling.[18−21] The morphology and structure of CNTS are observed by scanning electron microscopy (SEM) and transmission electron microscopy (TEM). It can be found that the as-synthesized CNTS shows flower-like hierarchical nanosheet structure (Figure 1b), and the thickness of these nanosheets are about 30 nm. Each of these CNTS nanosheets (CNTSNs) flowers is several hundred nanometers (Figure S1 and Figure 1c). The corresponding high-resolution TEM (HRTEM) image (Figure 1d) shows good crystallinity of the CNTSNs. The interplanar spacing of 0.31 and 0.27 nm are corresponding well with the (111) and (200) plane of CNTS. This result indicates that the nanosheets grow along the [111] and [200] direction. As seen from Figure 1a, the peak intensity of (111) is stronger than that of (200), revealing that the (111) plane is the preferred growth plane compared to the standard XRD pattern of CNTS. To further confirm elements distribution in CNTSNs, we carried out element mapping analysis (Figure 1e−h). The elemental mapping from the
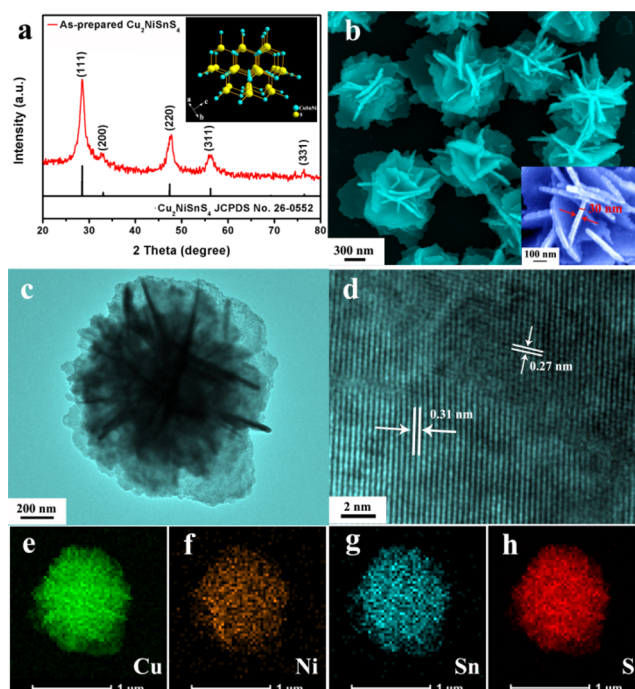
Figure 1. (a) XRD patterns of prepared and standard CNTS and (inset) the crystal structure of CNTS. (b) SEM image of as-prepared CNTSNs and (inset) high-resolution SEM image of as-prepared CNTSNs. (c) TEM image of as-prepared CNTSNs. (d) HRTEM image of CNTSNs. EDS characterization of CNTSNs (e) Cu, (f) Ni, (g) Sn, and (h) S mapping of CNTSNs shown in panel c.

Figure 1c clearly demonstrates that the obtained CNTSNs are only composed of Cu, Ni, Sn, and S, and these elements are evenly distributed. There is no noticeable compositional distribution among the nanosheets. No evidence of other binary or ternary compound in the obtained product is found, confirming the successful synthesis of pure phase CNTS.

To clearly figure out the growth mechanism of the hierarchical CNTSNs flowers, we investigated their growth process by XRD patterns and morphology variation. Figure 2a shows the XRD patterns of the obtained products in different solution concentration. These results clearly demonstrate that pure phase CNTS can be only obtained in the C_0 solution. Compared with the XRD patterns of C_0, some impurity peaks appeared in that of $C_0 1/3$, and parts of which can be indexed to CuS, $Cu_{1.92}S$. Similarly, when the solution concentration is increased to $C_0 5/3$ some impurity peaks appeared in the XRD patterns, some of which can be indexed to $Cu_2NiSn_3S_8$ except for CNTS. It should be noted that parts of these XRD peaks in $C_0 1/3$ and $C_0 5/3$ concentrations cannot be accurately indexed to any known phase according to the standard crystallographic database. To further investigate morphology of the CNTS in different solution concentrations, we took SEM images of these products after solvothermal reaction. When the solution concentration is $C_0 1/3$ (Figure 2c), the product is consists of nanosheets and nanospheres. For C_0, the obtained product is pure CNTS, which morphology comprises hierarchical nanosheet structure. When the concentration is raised to $C_0 5/3$, the obtained product is consisted of irregular nanospheres and nanoparticles, where no sheet-like structure can be observed.

We further investigated the purity of CNTS in C_0 solution concentration after different reaction time, as evidenced by XRD and SEM measurements. Figure 2e is the XRD patterns of
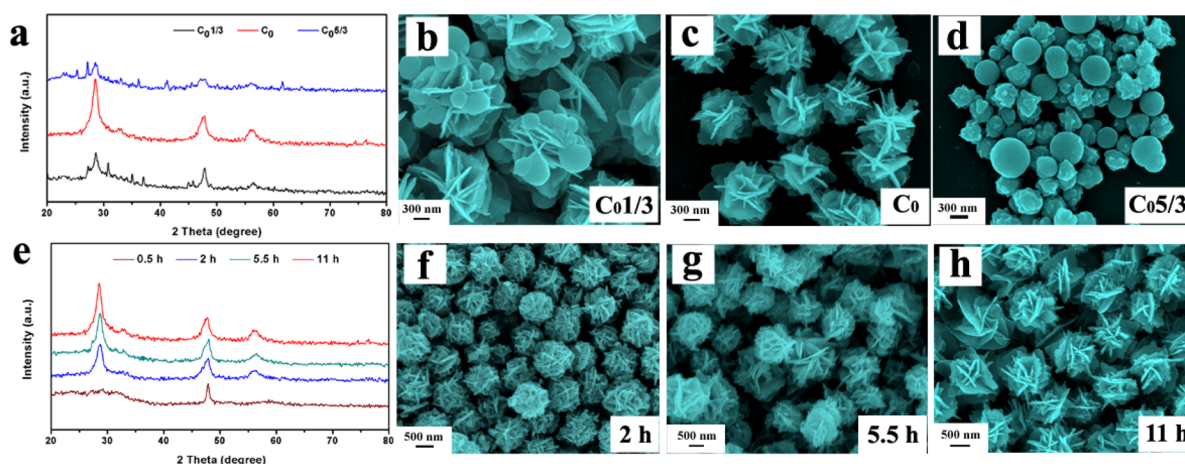
Figure 2. (a) XRD patterns of obtained products in different concentrate solution. (b−d) SEM images of the different products in panel a. (e) XRD patterns of the obtained products at different reaction time. (f−h) SEM images of the different products in panel e.

obtained products under 0.5, 2, 5.5, and 11 h, respectively; Figure 2f−h are the corresponding SEM images, respectively. After solvothermal reaction for 0.5 h, CuS (JCPDS 06-0464) peaks can be indexed. After the reaction time goes up to 2 h, the CNTS peaks can be found (Figure 2e). The dominant sphere-like product is agglomerated with numerous small nanosheets (Figure 2f), which is ca. 500 nm in diameter. When the reaction time is increased to 5.5 h, an impurity peak can also be seen at 31.44° (Figure 2e). Moreover, the morphology is changed to flower-like, which is consisted of thin nanosheets (Figure 2g). When the solvothermal reaction proceeds for 11 h, the impurity peak disappeared. Meanwhile, the obtained flowers are more uniformly distributed in size with thinner nanosheets.

On the basis of the above experiments, we propose a rational growth mechanism in C_0 concentration for the formation of 3D hierarchical flower-like CNTSNs and illustrate the preparation process of CNTSNs/RGNs in Figure 3. First, some of Cu^{2+}
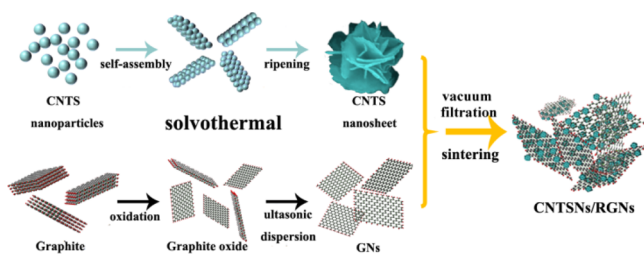
Figure 3. Schematic illustration of the preparation of CNTSNs, RGNs, and CNTSNs/RGNs compounds.

ions were reduced by H, which was induced by solvent or hydrated metal salt, to form Cu^+. Meanwhile, another part of Cu^{2+} ions were reacted with thiourea to form CuS ($Cu^{2+} + S^{2-} \rightarrow CuS$);[32−34] those products are in accordance with the above XRD result in Figure 2e. Then the CuS was aggregated with Cu^+, Ni^{2+}, and Sn^{2+} to form CNTS nucleus through the assembly process ($CuS + Cu^+ + Ni^{2+} + Sn^{4+} + 3S^{2-} \rightarrow Cu_2NiSnS_4$).[32−34] As the reaction time extended, the crystal nucleus grows up to different size particles, and further form 3D small nanosheets structures spontaneously (Figure 2f). However, the small nanosheets are unstable, which will be dissolved and further grow up to nanosheets through an oriented process.[32,33] Eventually, 3D hierarchical and flower-

like CNTS with thinner and smoother nanosheets structure is formed. The RGNs are prepared by Hummer's method. The CNTSNs/RGNs compounds are prepared by a facile vacuum filter method and then sintering in Ar atmosphere. Figure S2 shows the SEM image of the obtained RGNs. It should be noted that the size of the RGNs are large enough to cover different materials ranging in size from nanoscale to microscale, which is of critical importance to ensure that CNTSNs can be effectively covered or supported by RGNs. It is important that after integration with reduced RGNs, there is no change on crystallization of CNTSNs and the XRD patterns of CNTSNs/RGNs is shown in Figure S3. To determine whether the RGNs conductivity networks can improve the electrochemical properties, we examined the CNTSNs/RGNs composite anodes for NIBs using metal Na as counter electrodes. For comparison, bare CNTSNs are also tested under the same condition. Before electrochemical tests, SEM image of CNTSNs/RGNs and Raman spectra of CNTSNs/GNs and CNTSNs/RGNs were measured first. In Figure S4a, it can be clearly seen that a layer of RGNs is coated on the surface of CNTSNs homogeneously, while the CNTSNs still contained their original flower-like morphology. Such morphology characteristics are very beneficial when used as battery electrodes. Raman spectrum spectra of CNTSNs/GNs and CNTSNs/RGNs are showed in Figure S4b. Both of CNTSNs/GNs and CNTSNs/RGNs exhibit a broad disorder induced D-band (~1350 cm^{-1}) and an in-plane vibrational G-band (~1590 cm^{-1}).[35] The integral intensity ratio (I_G/I_D) is indicative of the degree of graphitic ordering in the carbons, and a high I_G/I_D value indicates more defects in the carbon structure.[36] After sintering treatment, the ratio of I_G/I_D is 0.88, which is higher than that of CNTSNs/GNs (0.79). This indicates that the sintering treatment increases defect sites in the graphene-based carbon and weakens the degree of sp^2-carbon, which would benefit the electron transport and the kinetic of subsequent Na^+ inertion/extraction reaction.[37] Thermogravimetric analysis (Figure S5) shows that the CNTSNs/RGNs composite contains ~90% CNTSNs and ~10% RGNs.

Figure 4a shows the discharge−charge profiles at a current density of 25 mA g^{-1} over the voltage range 0−3.0 V. The initial discharge capacity of CNTSNs/RGNs is 840 mAh g^{-1}, which is considerable high capacity among the anode materials of NIBs. Bare RGNs were also tested in Figure S6, and we can conclude that the RGNs contributed negligible capacity in
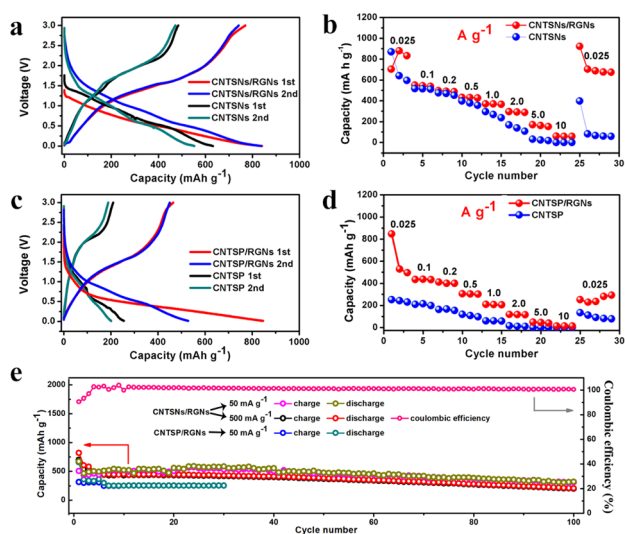
Figure 4. (a) Charge−discharge profiles of CNTSNs and CNTSNs/RGNs electrodes at a current density of 25 mA g^{-1}. (b) Rate capability of CNTSNs and CNTSNs/RGNs electrodes at various current densities from 0.025 to 10 A g^{-1}. (c) Charge−discharge profiles of CNTSP and CNTSP/RGNs electrodes at a current density of 25 mA g^{-1}. (d) Rate capability of CNTSP and CNTSP/RGNs electrodes at various current densities from 0.025 to 10 A g^{-1}. (e) Cycling performance of CNTSNs/RGNs and CNTSP/RGNs at 50 mA g^{-1} current density, cycling performance and Coulombic efficiency of CNTSNs/RGNs at 500 mA g^{-1} current density.

NIBs. The initial irreversible capacity of the composite could be attributed to form solid electrolyte interface (SEI) films on the surface of electrode which due to the electrolyte decomposition and the reaction of residual oxygen-containing functional groups on RGNs with Na$^+$ ions.[19,24] For bare CNTSNs, although a high initial discharge of 631 mAh g^{-1} can be obtained, the reversible discharge capacity is fast decreased to 552 mAh g^{-1}, which is much lower than that of CNTSNs/RGNs composite electrode. It should be noted that the addition of RGNs in CNTSNs/RGNs and CNTSP/RGNs could improve the electrical conductivity of electrodes, while discharge curves could be changed due to somewhat residual oxygen-containing functional groups of RGNs. Figure 4b demonstrates the rate capacity of CNTSNs/RGNs and bare CNTSNs electrodes at current densities from 0.025 to 10 A g^{-1}. Surprisingly, even at very high discharge current densities of 2/5/10 A g^{-1}, the CNTSNs/RGNs electrodes can still deliverer 296/171/61 mAh g^{-1} discharge capacity, respectively, which are much higher than bare CNTSNs electrode (168/31/0 mAh g^{-1}). Furthermore, after the ultrafast discharge test, a discharge capacity of 923 mAh g^{-1} can recover back for CNTSNs/RGNs electrode. This is much higher than that of bare CNTSNs (397 mAh g^{-1}), which further confirm the advantage of adding flexible conductive RGNs network in electrodes.

To further confirm the advantages of CNTSNs with nanostructure, we also tested CNTS powder with irregular morphology (CNTSP) and CNTSP/RGNs under the same condition. (The SEM images of CNTSP and CNTSP/RGNs are shown in Figure S7). As shown in Figure 4c, the initial discharge capacities of CNTSP/RGNs and CNTSP are 846 and 256 mAh g^{-1}, respectively. However, after the first cycle, the discharge capacities decreased rapidly to 528 and 201 mAh g^{-1}, respectively. Figure 4d shows rate capability of the CNTSP/

RGNs and bare CNTSP from 0.025 to 10 A g^{-1}. Although the discharge capacities of CNTSP/RGNs (118/49/14 mAh g^{-1}) are much higher than CNTSP (15/0/0 mAh g^{-1}) at current densities of 2/5/10 A g^{-1}, it is still much lower than that of the CNTSNs/RGNs electrode at the same current density. These results indicate the advantage of the CNTSNs with hierarchical nanostructure in NIBs adequately. Except for the ultrahigh rate capability, CNTSNs/RGNs also show good cycling stability. As shown in Figure 4e, the CNTSNs/RGNs composites exhibit higher specific capacity and better cycling stability than CNTSP/RGNs. After 100 cycles, the CNTSNs/RGNs composites still retain a high reversible capacity of ∼321 mAh g^{-1} at a current density of 50 mA g^{-1}, whereas after 20 cycles the CNTSP/RGNs electrode shows a specific capacity lower than 253 mAh g^{-1}. When tested at a high current density of 500 mA g^{-1}, CNTSNs/RGNs composites can also retain a high capacity of 207 mAh g^{-1} with a high Coulombic efficiency of nearly 100% even after 100 cycles. For further comparison, the cycling stability of bare CNTSNs and bare CNTSP electrodes were also tested (Figure S8). For the CNTSNs electrode, its capacity (131 mAh g^{-1}) is significantly lower than that of the CNTSNs/RGNs electrode after 30 cycles, while bare CNTSP electrode only shows 96 mAh g^{-1} after 30 cycles. The serious capacity fading can be attributed to the low electronic conductivity of CNTS and the unrestrained aggregations of Sn or Na$_x$Sn during cycling.[24,38] These results further demonstrate the advantages and feasibility for application of the combination of RGNs conductive network with 3D nanostructured materials in NIB electrodes.

To reveal the structure and phase change of the CNTSNs/RGNs electrode during the electrochemical reactions, cyclic voltammetry (CV) and ex situ XRD techniques were used. Figure 5a shows the CV curves of CNTSNs/RGNs at the 1st, 5th, and 10th cycles between 0 ∼ 3 V at a scan rate of 0.1 mV s^{-1}. During the first discharge process, this electrode shows two broad peaks at 1.4 and 0.75 V, which are corresponding to the formation of solid electrolyte interphase (SEI), and the multistep conversion of CNTS to metallic Cu, Ni, Sn and amorphous Na$_x$S matrix.[3,38,39] The Cu and Ni nanoparticles can improve the electrical contact with CNTS during cycling. When the voltage lowered to 0.5 V, more Na$^+$ intercalating in RGNs, and metallic Na−Sn nanoparticles are generated, which have been widely reported in Sn-based anode materials in NIBs.[3,24] During the charging process, a broad reduction peak at about 0.44 V is resulted from the deintercalation of Na$^+$ from Na−Sn alloy.[24,40] The peaks locate at 1.46, 1.70, and 1.91 V may correspond to the restitution of Sn−S, Cu−S, and the original CNTS. After the first cycle, such peaks can be also observed at the same potential range, indicating very good reversibility of CNTSNs/RGNs toward sodiation and desodiation reactions. Meanwhile, the good stability of the peaks suggests that RGNs have buffered the volume change during the alloy and dealloy reaction of Na and Sn. To investigate the phase evolution of CNTSNs/RGNs upon Na$^+$ insertion/extraction, we conducted ex situ XRD measurement on the CNTSNs/RGNs electrodes at different states (Figure 5b), wherein these states are corresponding to the points 1 to 6 in Figure 5a. When discharged to 1.0 V (line 1), nearly all the peaks of CNTS disappeared, indicating that complete consumption of CNTS to form amorphous products or ultrasmall particles. After discharged to 0.5 V (line 2), some new peaks of NaS, Na$_2$S$_5$ and SnS appeared. Interestingly, when discharged to 0 V (line 3), all of the peaks of Na−S and CNTS disappeared
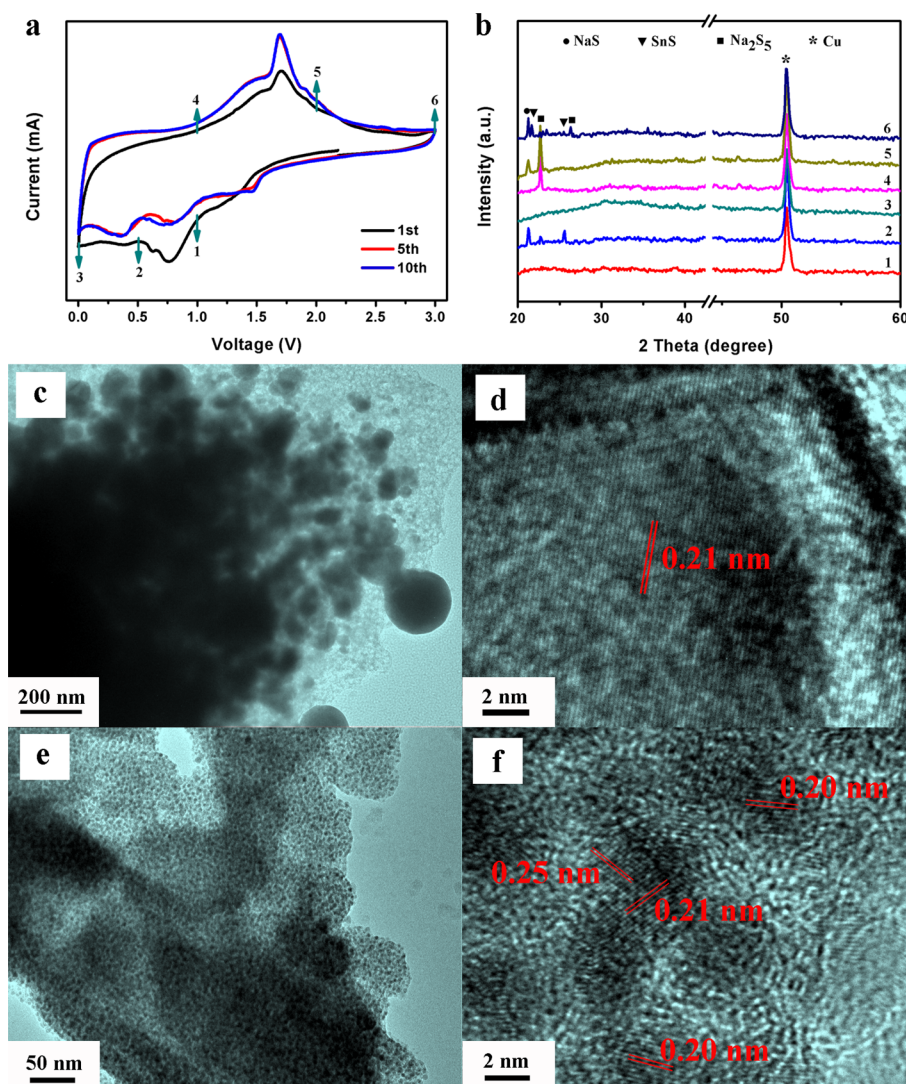
Figure 5. (a) CV curves of CNTSNs/RGNs electrode at a scan rate of 0.1 mV s^{-1} between 0 and 3.0 V. (b) Ex situ XRD patterns of CNTSNs/RGNs electrode at different charge−discharge states. (c, d) Different resolution TEM images of CNTSNs/RGNs electrode after discharged to 0 V. (e, f) Different resolution TEM images of CNTSNs/RGNs electrode after recharged to 3.0 V.

completely. But only Na−Sn peaks (∼30−32°) appeared, indicating that the Na−S compounds are reduced when Na−Sn alloy is generated. Additionally, most of these products show poor crystallinity or amorphous, which would benefit the kinetic of subsequent Na$^+$ insertion/extraction reaction.[41] During charging process, Na$_2$S$_5$ is first generated (line 4), followed by NaS (line 5). When recharged to 3.0 V, the peak of Na$_2$S$_5$ turns weaker, and some peaks of SnS and other unknown phases appeared. It is demonstrated that the recovered CNTS is amorphous or poor crystallinity. The morphology changes and the charge/discharge products are investigated by TEM. After discharged to 0 V (Figure 5c), a number of particles with large volume can be observed on RGNs. According to the electrochemical reaction mechanism, an overwhelming majority of these particles are Na−Sn alloy. From HRTEM image (Figure 5d), we can see that the interplanar spacing of the particle is 0.21 nm, which is well matched with the (611) plane of Na$_{15}$Sn$_4$. After recharged to 3.0 V (Figure 5e), these particles not only diminished significantly, but also uniformly distributed.

HRTEM image (Figure 5f) proves that these small particles are either Na−Sn alloy (0.21/0.25 nm) or Cu/Ni (0.20 nm). It demonstrates that there are some irreversible Na−Sn alloy and Cu/Ni nanoparticles residues in this electrode. Interestingly, these conductive nanoparticle matrix composed in the electrode are in ideal contact with the active component, which are beneficial for the improvement of battery performance.[42] Further study is needed on the mechanism of Na$^+$ insertion into and extraction from CNTS.

Combined with the high capacity, good cyclic performance, and ultrahigh rate capability, we believe that such composites of CNTSNs with RGNs are good candidate as anode materials of high-performance NIBs. The superior performance of the NIBs based on the CNTSNs/RGNs composite electrodes can be explained as follows: (1) The flexible RGNs in the composite not only provide an elastic buffer space to accommodate the volume expansion/contraction of CNTSNs during Na$^+$ insertion/extraction process but also efficiently prevent the crumbling of electrode material upon continuous charge−discharge process, thus maintaining high capacity and good cycling stability.[25−28] (2) The RGNs conductive networks in

the composite significantly decrease the inner resistance of NIBs and are favorable for stabilizing the electronic and ionic conductivity, therefore leading to a higher specific capacity.[25−28] The electrochemical impedance spectra of CNTSNs and CNTSNs/RGNs composites (Figure S9) confirmed that assembling with RGNs largely improves the electrochemical activity of CNTSNs. (3) The 3D hierarchical architecture CNTS combined with the tunneled and layered structure can not only provides a sufficient electrode/electrolyte contact area and short Na^+ ions transport length, but also facilitates continuous and fast conducting pathways for electrons and ions through the electrodes during the charging and discharging process, which could improve the battery performance greatly.[18−21,43−46] (4) Metal nanoparticles, such as Na_xSn or Cu/Ni, dispersed in the electrode would be an ideal conductive matrix to improve the batteries performance significantly.[41,42] According to the above analysis, we can conclude that the synergetic effect between conducting RGNs and 3D hierarchical CNTSNs is responsible and inevitable for the outstanding electrochemical performances via the maximum utilization of electrochemically active CNTSNs and good electrical conductivity RGNs.

CONCLUSION

In conclusion, the self-assembly 3D hierarchically structural flower-like CNTSNs and CNTSNs/RGNs are prepared by a facile, low cost, and time-saving strategy. The as-synthesized CNTSNs/RGNs composites demonstrate and highlight the effectiveness of combining conductivity and flexibility in a component to improve the electrochemical performance for NIBs. In contrast to bare CNTSNs, the CNTSNs/RGNs composite shows a significantly improved discharge capacity and rate capability than that of the bare CNTSNs in NIBs anodes. Because CNTSNs/RGNs have a high reversible capacity of 837 mAh g^{-1}, good cycle stability and rate capability even at 10 A g^{-1}, which are superior over its bare CNTSNs and CNTS particles counterparts.

ASSOCIATED CONTENT

⑤ Supporting Information

The Supporting Information is available free of charge on the ACS Publications website at DOI: 10.1021/acsami.6b01725.

Experimental procedure and the results from TEM, SEM, Raman spectra, TG curves, electrochemical test. (PDF)

AUTHOR INFORMATION

Corresponding Authors
*E-mail: xbzhang@ciac.ac.cn.
*E-mail: junminyan@jlu.edu.cn.

Author Contributions
§These authors contributed equally to this work.

Notes
The authors declare no competing financial interest.

ACKNOWLEDGMENTS

REFERENCES

(1) Wang, Y.; Wei, M.; Fan, F.; Zhuang, T.; Wu, L.; Yu, S. H.; Zhu, C. F. Phase-Selective Synthesis of Cu_2ZnSnS_4 NanoCrystals through Cation Exchange for Photovoltaic Devices. *Chem. Mater.* **2014**, *26*, 5492−5498.

(2) Zhao, J.; Bardecker, J. A.; Munro, A. M.; Liu, M. S.; Niu, Y.; Ding, I.; Luo, J.; Chen, B.; Jen, A. K.; Ginger, D. S. Efficient CdSe/CdS Quantum Dot Light-Emitting Diodes Using A Thermally Polymerized Hole Transport Layer. *Nano Lett.* **2006**, *6*, 463−467.

(3) Qu, B.; Zhang, M.; Lei, D.; Zeng, Y.; Chen, Y.; Chen, L.; Li, Q.; Wang, Y.; Wang, T. H. Facile Solvothermal Synthesis of Mesoporous Cu_2SnS_3 Spheres and Their Application in Lithium-Ion Batteries. *Nanoscale* **2011**, *3*, 3646−3651.

(4) Cui, Y.; Deng, R.; Wang, G.; Pan, D. C. A General Strategy for Synthesis of Quaternary Semiconductor Cu_2MSnS_4 (M= Co^{2+}, Fe^{2+}, Ni^{2+}, Mn^{2+}) Nanocrystals. *J. Mater. Chem.* **2012**, *22*, 23136−23140.

(5) Wang, T. X.; Li, Y.; Liu, H.; Li, H.; Chen, S. Flower-Like Cu_2NiSnS_4 Nanoparticles Synthesized by A Facile Solvothermal Method. *Mater. Lett.* **2014**, *124*, 148−150.

(6) Kamble, A.; Mokurala, K.; Gupta, A.; Mallick, S.; Bhargava, P. Synthesis of Cu_2NiSnS_4 Nanoparticles by Hot Injection Method for Photovoltaic Applications. *Mater. Lett.* **2014**, *137*, 440−443.

(7) Reddy, M. V.; Subba Rao, G. V. S.; Chowdari, B. V. R. Metal Oxides and Oxysalts as Anode Materials for Li Ion Batteries. *Chem. Rev.* **2013**, *113* (7), 5364−5457.

(8) Yang, Y.; Zheng, G.; Cui, Y. Nanostructured Sulfur Cathodes. *Chem. Soc. Rev.* **2013**, *42*, 3018−3032.

(9) Melot, B. C.; Tarascon, J. M. Design and Preparation of Materials for Advanced Electrochemical Storage. *Acc. Chem. Res.* **2013**, *46*, 1226−1238.

(10) Zhang, Q. F.; Uchaker, E.; Candelaria, S. L.; Cao, G. Z. Nanomaterials for Energy Conversion and Storage. *Chem. Soc. Rev.* **2013**, *42*, 3127−3171.

(11) Wang, J. J.; Li, Y. L.; Sun, X. L. Challenges and Opportunities of Nanostructured Materials for Aprotic Rechargeable Lithium−Air Batteries. *Nano Energy* **2013**, *2*, 443−467.

(12) Wu, J. S.; Rui, X. H.; Wang, C. Y.; Pei, W. B.; Lau, R.; Yan, Q. Y.; Zhang, Q. C. Nanostructured Conjugated Ladder Polymers for Stable and Fast Lithium Storage Anodes with High-Capacity. *Adv. Energy Mater.* **2015**, *5*, 1402189.

(13) Yu, Y.; Gu, L.; Zhu, C.; van Aken, P. A.; Maier, J. Tin Nanoparticles Encapsulated in Porous Multichannel Carbon Microtubes: Preparation by Single-Nozzle Electrospinning and Application as Anode Material for High-Performance Li-Based Batteries. *J. Am. Chem. Soc.* **2009**, *131*, 15984−15985.

(14) Park, Y. U.; Seo, D. H.; Kwon, H. S.; Kim, B.; Kim, J.; Kim, H.; Kim, I.; Yoo, H.; Kang, K. A New High-Energy Cathode for A Na-Ion Battery with Ultrahigh Stability. *J. Am. Chem. Soc.* **2013**, *135*, 13870−13878.

(15) Qian, J. F.; Xiong, Y.; Cao, Y. L.; Ai, X.; Yang, H. X. Synergistic Na-Storage Reactions in Sn_4P_3 as A High-Capacity, Cycle-Stable Anode of Na-Ion Batteries. *Nano Lett.* **2014**, *14*, 1865−1869.

(16) Wang, S. W.; Wang, L. J.; Zhu, Z. Q.; Hu, Z.; Zhao, Q.; Chen, J. All Organic Sodium-Ion Batteries with $Na_4C_8H_2O_6$. *Angew. Chem., Int. Ed.* **2014**, *53*, 5892−5896.

(17) Luo, C.; Xu, Y.; Zhu, Y.; Liu, Y.; Zheng, S.; Liu, Y.; Langrock, A.; Wang, C. S. Selenium@ Mesoporous Carbon Composite with Superior Lithium and Sodium Storage Capacity. *ACS Nano* **2013**, *7*, 8003−8010.

(18) Yabuuchi, N.; Kajiyama, M.; Iwatate, J.; Nishikawa, H.; Hitomi, S.; Okuyama, R.; Usui, R.; Yamada, Y.; Komaba, S. P2-type $Na_x[Fe_{1/2}Mn_{1/2}]O_2$ Made from Earth-Abundant Elements for Rechargeable Na Batteries. *Nat. Mater.* **2012**, *11*, 512−517.

(19) Pan, H. L.; Hu, Y. S.; Chen, L. Q. Room-Temperature Stationary Sodium-Ion Batteries for Large-Scale Electric Energy Storage. *Energy Environ. Sci.* **2013**, *6*, 2338−2360.

(20) Su, D.; Wang, G. X. Single-Crystalline Bilayered V_2O_5 Nanobelts for High-Capacity Sodium-Ion Batteries. *ACS Nano* **2013**, *7*, 11218−11216.

(21) Yuan, S.; Liu, Y.; Xu, D.; Ma, D.; Wang, S.; Yang, X.; Cao, Z.; Zhang, X. B. Pure Single-Crystalline $Na_{1.1}V_3O_{7.9}$ Nanobelts as Superior Cathode Materials for Rechargeable Sodium-Ion Batteries. *Adv. Sci.* **2015**, *2*, 1400018.

(22) David, L.; Bhandavat, R.; Singh, G. MoS_2/Graphene Composite Paper for Sodium-Ion Battery Electrodes. *ACS Nano* **2014**, *8*, 1759−1770.

(23) Zhu, C.; Mu, X.; van Aken, P. A.; Yu, Y.; Maier, J. Single-Layered Ultrasmall Nanoplates of MoS_2 Embedded in Carbon Nanofibers with Excellent Electrochemical Performance for Lithium and Sodium Storage. *Angew. Chem., Int. Ed.* **2014**, *53*, 2152−2156.

(24) Qu, B.; Ma, C.; Ji, G.; Xu, C.; Xu, J.; Meng, Y. S.; Wang, T. H.; Lee, J. Y. Layered SnS_2-Reduced Graphene Oxide Composite-A High-Capacity, High-Rate, and Long-Cycle Life Sodium-Ion Battery Anode Material. *Adv. Mater.* **2014**, *26*, 3854−3859.

(25) Yu, Z.; Song, J.; Gordin, M. L.; Yi, R.; Tang, D.; Wang, D. H. Phosphorus-Graphene Nanosheet Hybrids as Lithium-Ion Anode with Exceptional High-Temperature Cycling Stability. *Adv. Sci.* **2015**, *2*, 1400020.

(26) Huang, Y.; Huang, X.; Lian, J.; Xu, D.; Wang, L. M.; Zhang, X. B. Self-assembly of Ultrathin Porous NiO Nanosheets/Graphene Hierarchical Structure for High-Capacity and High-Rate Lithium Storage. *J. Mater. Chem.* **2012**, *22*, 2844−2847.

(27) Huang, X. L.; Wang, R.; Xu, D.; Wang, Z.; Wang, H.; Xu, J.; Wu, Z.; Liu, Q.; Zhang, Y.; Zhang, X. B. Homogeneous CoO on Graphene for Binder-Free and Ultralong-Life Lithium Ion Batteries. *Adv. Funct. Mater.* **2013**, *23*, 4345−4353.

(28) Gao, G.; Wu, H. B.; Dong, B.; Ding, S.; Lou, X. W. Growth of Ultrathin $ZnCo_2O_4$ Nanosheets on Reduced Graphene Oxide with Enhanced Lithium Storage Properties. *Adv. Sci.* **2015**, *2*, 1400014.

(29) Chae, C.; Noh, H.; Lee, J. K.; Scrosati, B.; Sun, Y. K. A High-Energy Li-Ion Battery Using a Silicon-Based Anode and a Nano-Structured Layered Composite Cathode. *Adv. Funct. Mater.* **2014**, *24*, 3036−3042.

(30) Prabakar, S. J. R.; Hwang, Y.; Bae, E.; Shim, S.; Kim, D.; Lah, M. S.; Sohn, K. S.; Pyo, M. SnO_2/Graphene Composites with Self-Assembled Alternating Oxide and Amine Layers for High Li-Storage and Excellent Stability. *Adv. Mater.* **2013**, *25*, 3307−3312.

(31) Li, J.; Shen, J.; Li, Z.; Li, X.; Sun, Z.; Hu, Z.; Huang, S. Wet chemical Route to the Synthesis of Kieserite Cu_2ZnSnS_4 Nanocrystals and Their Applications in Lithium Ion Batteries. *Mater. Lett.* **2013**, *92*, 330−333.

(32) Zhou, Y.; Zhou, W.; Li, M.; Du, Y.; Wu, S. Hierarchical Cu_2ZnSnS_4 Particles for a Low-Cost Solar Cell: Morphology Control and Growth Mechanism. *J. Phys. Chem. C* **2011**, *115*, 19632−19639.

(33) Chen, F.; Zai, J.; Xu, M.; Qian, X. F. 3D-hierarchical Cu_3SnS_4 Flowerlike Microspheres: Controlled Synthesis, Formation Mechanism and Photocatalytic Activity for H_2 Evolution from Water. *J. Mater. Chem. A* **2013**, *1*, 4316−4323.

(34) Sarkar, S.; Bhattacharjee, K.; Das, G. C.; Chattopadhyay, K. K. Self-Sacrificial Template Directed Hydrothermal Route to Kesterite-Cu_2ZnSnS_4 Microspheres and Study of Their Photo Response Properties. *CrystEngComm* **2014**, *16*, 2634−2644.

(35) Choi, C. H.; Park, S. H.; Woo, S. I. Binary and Ternary Doping of Nitrogen, Boron, and Phosphorus into Carbon for Enhancing Electrochemical Oxygen Reduction Activity. *ACS Nano* **2012**, *6*, 7084−7091.

(36) Yang, S.; Zhi, L.; Tang, K.; Feng, X.; Maier, J.; Müllen, K. Efficient Synthesis of Heteroatom (N or S)-Doped Graphene Based on Ultrathin Graphene Oxide-Porous Silica Sheets for Oxygen Reduction Reactions. *Adv. Funct. Mater.* **2012**, *22*, 3634−3640.

(37) Yao, F.; Güneş, F.; Ta, H. Q.; Lee, S. M.; Chae, S. J.; Sheem, K. Y.; Cojocaru, C. S.; Xie, S. S.; Lee, Y. H. Diffusion Mechanism of Lithium Ion through Basal Plane of Layered Grapheme. *J. Am. Chem. Soc.* **2012**, *134*, 8646−8654.

(38) Zhang, Z.; Zhou, C.; Jia, M.; Fu, Y.; Li, J.; Lai, Y. Synthesis of Copper Tin Sulfide/Reduced Graphene Oxide Composites and Their Electrochemical Properties for Lithium Ion Batteries. *Electrochim. Acta* **2014**, *143*, 305−311.

(39) Yang, X.; Xu, J.; Xi, L.; Yao, Y.; Yang, Q.; Chung, C. Y.; Lee, C. Microwave-Assisted Synthesis of Cu_2ZnSnS_4 Nanocrystals as A Novel Anode Material for Lithium Ion Battery. *J. Nanopart. Res.* **2012**, *14*, 1−6.

(40) Ellis, L. D.; Hatchard, T. D.; Obrovac, M. N. Reversible Insertion of Sodium in Tin. *J. Electrochem. Soc.* **2012**, *159*, A1801−A1085.

(41) Bruce, P. G.; Scrosati, B.; Tarascon, J. M. Nanomaterials for Rechargeable Lithium Batteries. *Angew. Chem., Int. Ed.* **2008**, *47*, 2930−2946.

(42) Kirshenbaum, K.; Bock, D. C.; Lee, C.-Y.; Zhong, Z.; Takeuchi, K. J.; Marschilok, A. C.; Takeuchi, E. S. In Situ Visualization of Li/$Ag_2VP_2O_8$ Batteries Revealing Rate-Dependent Discharge Mechanism. *Science* **2015**, *347*, 149−154.

(43) Jiang, J.; Li, Y.; Liu, J.; Huang, X.; Yuan, C.; Lou, X. W. Recent Advances in Metal Oxide-Based Electrode Architecture design for Electrochemical Energy Storage. *Adv. Mater.* **2012**, *24*, 5166−5180.

(44) Lee, K. T.; Cho, J. Roles of Nanosize in Lithium Reactive Nanomaterials for Lithium Ion Batteries. *Nano Today* **2011**, *6*, 28−41.

(45) Mahmood, N.; Hou, Y. L. Electrode Nanostructures in Lithium-Based Batteries. *Adv. Sci.* **2014**, *1*, 1400012.

(46) Nowack, L. V.; Bunjaku, T.; Wegner, K.; Pratsinis, S. E.; Luisier, M.; Wood, V. Design and Fabrication of Microspheres with Hierarchical Internal Structure for Tuning Battery Performance. *Adv. Sci.* **2015**, *2*, 1500078.